A Self-Consistent Numerical Treatment of Fractal Aggregate Dynamics

Derek C. Richardson

*Canadian Institute for Theoretical Astrophysics, McLennan Labs, University of Toronto, 60 St. George Street,
Toronto, Ontario, Canada M5S 1A7*
E-mail: richards@cita.utoronto.ca

A self-consistent numerical treatment for modeling fractal aggregate dynamics is presented. Fractal aggregates play an important role in a number of complex astrophysical regimes, including the early solar nebula and the interstellar medium. Aggregates can be of various forms and sizes, ranging from tiny dust particles to ice chunks in planetary rings and possibly even comets. Many observable properties, such as light scattering and polarization, may depend sensitively on the geometry and motion of such aggregates. Up to now various statistical methods have been used to model the growth and interaction of aggregates. The method presented here is unique in that a full treatment of rigid body dynamics—including rotation—is incorporated, allowing individual particle and cluster trajectories and orientations to be followed explicitly. The method involves solving Euler's equations for rigid body motion and introducing a technique for handling oblique collisions between arbitrarily shaped aggregates. Individual particles may be of any size and can have their own spin. Currently tangential impulses during impacts are assumed negligible, although equations for the treatment of tangential friction are presented. Models for the coagulation and restitution of aggregates are discussed in detail. Some of the key features required for a fragmentation model, not implemented here, are discussed briefly. Torque effects arising from self-gravity, tidal fields, or gas drag are not presently considered. Although the discussion focuses mainly on the theory behind the numerical technique, test simulations are presented to compare with an analytic solution of the coagulation equation and to illustrate the important aspects of the method. © 1995 Academic Press, Inc.

1. INTRODUCTION

The importance of fractal aggregate dynamics in astrophysical systems dominated by gas and dust is becoming increasingly recognized. In the present context, an aggregate is a heterogeneous collection of particles fused together through mutual inelastic collisions. An aggregate may also refer to a body made up of individual fragments held together by mutual self-gravity. A solid aggregate is said to be fractal if its geometry is such that the density of constituents falls off as some nonzero inverse power of the radius. Hence fractal aggregates are "fluffy" and consequently, if the mass is sufficiently small, may be able to couple with any gas in their environment very easily (e.g., Meakin and Donn 1988).

It has long been thought that gravitational instability alone in the solar nebula could explain the rapid growth of planetesimals (Safronov 1969, Goldreich and Ward 1973). But recent work (Weidenschilling et al. 1989, Cuzzi et al. 1993, Weidenschilling and Cuzzi 1993) suggests that turbulence may have prevented the onset of gravitational instability until meter-sized or larger particles had been formed through unfocused binary accretion. In this case mutual collisions were driven by turbulence in the gas or by relative velocities arising from drift rates that varied depending on particle size. It is likely that the resulting accretion was ballistic in nature; that is, the mean free path between collisions exceeded the mean particle size. A variety of physical and numerical experiments have shown that such aggregation leads naturally to the formation of fractal aggregates (e.g., Blum and Münch 1993, Blum et al. 1994). Current studies of stars such as β Pictoris that are observed to have circumstellar material promise to yield further insights into the dynamical properties of primordial gas and dust (see, e.g., Backman and Paresce 1993).

The only physical evidence that exists today in our Solar System regarding the nature of early aggregates can be found in primitive meteorites. These bodies are abundantly speckled with millimeter- to centimeter-sized "chondrules" whose origins are still largely unknown (Grossman 1988, Palme and Boynton 1993). However, it is generally accepted that solid clumps of material had to be heated and cooled rapidly in order to form the chondrules (e.g., Boss and Graham 1993). Many theories of the heating and cooling mechanisms have been put forward, but it is likely that a better understanding of aggregate dynamics would improve the picture.

Aggregates need not all be tiny clumps of dust particles. Recent numerical work on Saturn's rings (Richard-

son 1994, Salo 1994) has shown that aggregates can readily form in the dense regions of the outer main rings, where the constituent particles are inferred to be chunks of water ice ranging in size from ~1 cm to several meters in size (Cuzzi et al. 1984). Some of these particles may stick due to cohesion between surface frost layers (Hatzes et al. 1991), though this process was not modeled in the cited simulations. The aggregate formation is driven by gravitational instability, despite the strong tidal field of the planet. The associations typically persist for a few orbital periods before breaking up. The presence of these aggregates and associated gravitational wakes may explain the observed azimuthal brightness asymmetry of the A ring (Lumme and Irvine 1979). Their presence is also consistent with recent results from a Voyager photopolarimeter experiment (Showalter and Nicholson 1990).

Recent world attention on the spectacular impact of Comet Shoemaker–Levy 9 with Jupiter has focused interest on aggregation processes even more. Weidenschilling (1994), Asphaug and Benz (1994), Solem (1994), and others proposed models for the nature of the comet fragments, suggesting that some of the fragments themselves may be loosely bound aggregates (earlier work in this area can be found in Donn 1990). It will be very interesting to see the quantitative measurements arising from this once-in-a-millenium event, which may shed further light on the nature of these larger gravitational aggregates.

Numerical simulations of small-particle aggregation in astrophysical contexts generally employ statistical methods, such as Monte Carlo techniques, to build aggregates in free space by solving the coagulation equation (Liffman 1992) or by shooting particles or clusters at a nucleus fixed in a lattice (e.g., Ossenkopf 1993, Blum et al. 1994). Although a large number of particles ($N \gtrsim 10^4$) can be simulated using these methods, the principal disadvantage of these techniques is that they are not dynamically self-consistent. That is, the details of restitution and solid body rotation are not taken into account. Also, typical lattice simulations are divided into two regimes: particle–cluster aggregation (PCA) and cluster–cluster aggregation (CCA). In PCA simulations, aggregates are formed one particle at a time; in CCA, aggregates of identical size are merged to form larger aggregates. It is likely that the actual aggregation process that takes place in the solar nebula (for example) consists of a combination of these two extremes, probably dominated by the coagulation of subclusters of *different* size. The configuration of the final aggregate may depend sensitively on the dynamics of the subclusters. For example, if energy equipartition takes place in the system, then the larger an aggregate, the more likely it is to move and spin at a slower rate. In order to investigate these effects, it is necessary to adopt a more self-consistent, though much more computationally intensive, approach. It is not clear how important these details will turn out to be in astrophysical systems where particle aggregation is taking place. Nevertheless, it is now possible to model these effects, and numerical experiments that use these methods may prove valuable in future investigations.

Section 2 of this paper details a new particle-in-a-box method for modeling aggregate dynamics in free space. The aggregate constituents are uniform spheres and can be of arbitrary size. Spheres are chosen because their inherent symmetry makes them the simplest geometric objects to handle, both for computing inertia tensors and for detecting collisions. However, the basic theory is fully general and can be applied to more arbitrary shapes. In the current study, which focuses on the underlying numerical method, effects of mutual gravitation and gas drag are not considered. These effects and other interesting phenomena will be addressed in future projects.

Note that both aggregates and their constituents (the basic building blocks of the aggregates) are referred to interchangeably as "particles" in the text. This is because, on its own, an aggregate has many of the properties of a single particle located at the center of mass, and indeed the numerical method described here takes advantage of this. It should be clear from the context whether a "particle" refers to a single building block or an aggregate. The term "cluster" is also occasionally used to refer to an aggregate.

Results of test simulations performed with the new code are presented in Section 3 and compared with an analytic solution of the coagulation equation. A modified version of the box_tree code discussed in detail in Richardson (1993, 1994) was used for the simulations. Properties of the aggregates formed in the simulations are presented and discussed in this section. A summary of the conclusions follows in Section 4.

2. THEORY AND SIMULATION METHOD

The aggregate simulation method described here recognizes three possible collision outcomes: coagulation, restitution, and fragmentation. All three processes can involve single particles, a single particle and a cluster (aggregate), or two clusters. In the test simulations (Section 3), only coagulation and restitution are considered, and the choice of collision outcome depends only on the impact energy for simplicity. The treatment of each process is described below, together with a full description of the mathematical formalism and numerical tools needed to carry out the simulations.

2.1. Aggregate Properties

There are many aggregate properties that are useful to characterize. Dynamically, the most important are the moments of inertia, the principal axes, and the angular

velocity (spin). There are other properties that affect the dynamics of an aggregate but which are context dependent. These include the ratio of projected surface area to mass (important for gas drag), and the surface charge (important for dust-like aggregates). A helpful universal parameter that can be used to characterize the geometry of a given aggregate is the fractal dimension f_D, defined later.

For this initial study, only context-independent dynamical properties are of interest. These properties are also independent of the center of mass motion. Much of the treatment that follows is based on Chapter 5 of Goldstein (1980), which the reader may find to be a helpful review. The discussion of properties ends with a brief note on the computer representation of an aggregate.

2.1.1. The inertia tensor.

The inertia tensor **I** relates the spin angular momentum **h** of a rigid body to its angular velocity ω: $\mathbf{h} \equiv \mathbf{I}\omega$. Using the parallel axis theorem, the inertia tensor of an arbitrary aggregate of spheres is given by

$$\mathbf{I}_{agg} = \sum_i [\mathbf{I}_i + m_i(r_i^2 \mathbf{1} - \mathbf{r}_i \mathbf{r}_i)], \qquad (1)$$

where $\mathbf{I}_i = \frac{2}{5} m_i R_i^2 \mathbf{1}$ is the inertia tensor with respect to any diameter of a single sphere of mass m_i and radius R_i (**1** is the unit matrix). Each sphere i is located at a position $\mathbf{r}_i$ with respect to the center of mass of the aggregate.

Note that the inertia tensor is a real, symmetric matrix, that is, $\mathbf{I}^T = \mathbf{I}$, where superscript T denotes the transpose operator. This makes it particularly simple to diagonalize **I** (see below). Furthermore, **I** is always invertible.

2.1.2. Principal axes of an aggregate.

For any rigid body, there exists an orthogonal coordinate system in which the inertia tensor is diagonal. This coordinate system, denoted by the principal axes $\hat{\mathbf{p}}_i$, $i = 1, 2, 3$, can be found by diagonalizing **I** in the usual way (e.g., Press et al. 1992, Section 11.1–11.3). The eigenvectors of the inertia tensor are the principal axes, and the eigenvalues (the nonzero elements of the diagonal matrix) are the principal moments of inertia. Many operations are simplified by working in the body frame. For example, the rotational component of the kinetic energy of an aggregate is simply given by

$$T = \frac{1}{2} I_1 \omega_1^2 + \frac{1}{2} I_2 \omega_2^2 + \frac{1}{2} I_3 \omega_3^2, \qquad (2)$$

where I_i, $i = 1, 2, 3$, are the principal moments of inertia and the ω_i's are the spin components measured with respect to the body axes. The spin components in the fixed space frame can be obtained by a simple transformation: if **A** is a matrix whose columns are $\hat{\mathbf{p}}_1$, $\hat{\mathbf{p}}_2$, and $\hat{\mathbf{p}}_3$, then $\omega_{space} = \mathbf{A}\omega_{body}$. Since the transformation matrix is orthogonal, the operation is equivalent to a rotation. This transformation can be used with any vector quantity measured in the body frame. For example, the angular momentum in body coordinates due to rotation of an aggregate is given by

$$\mathbf{h}_{body} = (I_1\omega_1, I_2\omega_2, I_3\omega_3). \qquad (3)$$

The angular momentum as seen in the space frame is then $\mathbf{h}_{space} = \mathbf{A}\mathbf{h}_{body}$. Finally, note that since **A** is orthogonal (i.e., its column vectors form an orthonormal set), it is invertible and its inverse is equal to its transpose. Thus for any vector **x**, $\mathbf{x}_{space} = \mathbf{A}\mathbf{x}_{body}$ and $\mathbf{x}_{body} = \mathbf{A}^T\mathbf{x}_{space}$. From now on, **A** will denote the matrix whose columns are the principal axes.

2.1.3. Computer representation.

The computer representation of an aggregate poses a bit of a challenge, since it is necessary to keep track of the orientation of each component sphere. The simplest implementation is to represent each aggregate by a linked list of its basic building blocks, the first member of which contains all the center of mass information, such as position, velocity, time-step data for integration, and various statistics. This root particle structure also contains the principal moments of inertia of the entire aggregate, the principal axes (i.e., the orientation of the body as a whole), and the location in memory of the first member particle. The member particle structures need only contain minimal information: the position of the sphere center in body coordinates, the mass and radius, optional orientation information (useful for animations if the sphere has a surface pattern), and the memory location of the next member. The advantage of this setup is that the center of mass particle and a single, unaggregated particle share the same data structure, so that integration of (linear) particle movement need not distinguish between simple and aggregate particles. This means that linear and rotational motions are decoupled in the program (at least in the zero-torque case), greatly simplifying the numerical treatment.

2.2. Rigid Body Equations of Motion

The exact orientation of an aggregate is needed in order to detect collisions accurately. In two dimensions this is straightforward since rotational motion of aggregates in 2D can be characterized by a scalar angular velocity that remains constant between collsions. In 3D the problem becomes considerably more complex because the angular velocity vector is no longer constant: it can affect the orientation of the principal axes which in turn changes the angular velocity, leading to such phenomena as free precession. This complication is well known in rigid body dynamics and can be treated with a combination of Euler's equations and some vector calculus.

2.2.1. Euler's equations. The rotational motion of a rigid body is governed by Euler's equations

$$I_1\dot{\omega}_1 - \omega_2\omega_3(I_2 - I_3) = N_1,$$

$$I_2\dot{\omega}_2 - \omega_3\omega_1(I_3 - I_1) = N_2, \qquad (4)$$

$$I_3\dot{\omega}_3 - \omega_1\omega_2(I_1 - I_2) = N_3,$$

where I_i and ω_i have the usual definitions, and the N_i's are the principal axis components of any net torque acting on the body. In the absence of any net torques, Euler's equations reduce to

$$I_1\dot{\omega}_1 = \omega_2\omega_3(I_2 - I_3),$$

$$I_2\dot{\omega}_2 = \omega_3\omega_1(I_3 - I_1), \qquad (5)$$

$$I_3\dot{\omega}_3 = \omega_1\omega_2(I_1 - I_2),$$

which is a set of three linear, coupled, first-order differential equations. Such systems can readily be solved using standard numerical techniques (e.g., Press *et al.* 1992, Section 16.1: "Runge–Kutta Method"). The solution gives the angular velocity of the body as a function of time.

2.2.2. Motion of the principal axes. Although Eq. (5) fully describes the evolution of the angular velocity of a rigid body with respect to the body axes, more differential equations are required in order to calculate the spin as seen in the fixed space frame. This is because the principal axes will themselves move with respect to the space axes as the system evolves in time. To see this, consider a point **r** fixed in the body. Since the principal axes form a three-dimensional basis set, **r** can be expressed in the body coordinates $\mathbf{r} = r_1\hat{\mathbf{p}}_1 + r_2\hat{\mathbf{p}}_2 + r_3\hat{\mathbf{p}}_3$. Let $\boldsymbol{\omega}$ be the instantaneous angular velocity of the body as seen in the space frame, so that $\boldsymbol{\omega} = \omega_1\hat{\mathbf{p}}_1 + \omega_2\hat{\mathbf{p}}_2 + \omega_3\hat{\mathbf{p}}_3$. Then the instantaneous velocity of the point at **r** due to rotation is given by $\mathbf{v} = \boldsymbol{\omega} \times \mathbf{r}$ as seen in the space frame. To see how the first principal axis moves in time, set $r_1 = 1, r_2 = r_3 = 0$ (viz., a point at unit distance on the $\hat{\mathbf{p}}_1$ axis) and expand the cross product. Repeat the procedure for axes 2 and 3 to obtain

$$\dot{\hat{\mathbf{p}}}_1 = \omega_3\hat{\mathbf{p}}_2 - \omega_2\hat{\mathbf{p}}_3,$$

$$\dot{\hat{\mathbf{p}}}_2 = \omega_1\hat{\mathbf{p}}_3 - \omega_3\hat{\mathbf{p}}_1, \qquad (6)$$

$$\dot{\hat{\mathbf{p}}}_3 = \omega_2\hat{\mathbf{p}}_1 - \omega_1\hat{\mathbf{p}}_2.$$

Since these are vector equations, they introduce 9 new variables, making 12 in all (i.e., 9 axis components plus 3 spin components). Fortunately, these equations are of the same type as Euler's equations, namely linear and first order, so they can be handled easily by a standard differential equation solver.

Note that it was not necessary to invoke the cumbersome machinery of Euler angles to solve this problem (e.g., Klavetter 1989). Not only does this make the solution easier to understand, but it saves considerable CPU expense during simulations since complicated trigonometric operations are not required.

2.3. Collision Detection

Binary collision detection is an essential part of dynamical simulations of small bodies since dissipative collisions provide a balance for any energy input from orbital motions. In practice, a collision is detected only after the two bodies concerned just start to overlap. In Richardson (1994), a careful procedure was outlined to correct for such overlaps. However, in the absence of self-gravity, these overlaps ($\lesssim 1\%$) can safely be neglected.

To minimize overlaps, however, particle/cluster time steps should be chosen so that potential colliders are treated more carefully than particles or clusters that are far apart. This is easily accomplished by choosing $\Delta t = \eta(r/v)$, where r is the distance to the closest *approaching* particle or cluster and v is the relative velocity. The constant η is set at run time and should be less than unity (typically about 0.1–0.01). These time steps are used in a modified version of the individual time-step integration method of Aarseth (1985) to advance the particles.

Aggregates present a special problem for collision detection because of their arbitrary shapes. The procedure used in the current study is to assign a maximum size to each aggregate and store the value in the root particle radius variable. The maximum size is given by

$$R_{\max} = \max_i(r_i + R_i), \qquad (7)$$

where r_i is the distance of sphere i from the aggregate center and R_i is the sphere radius. If the distance between the centers of two aggregates is less than the sum of the corresponding maximum radii, then the aggregate orientations are updated (cf. Section 2.2) and a particle-by-particle check is performed to see if any part of the aggregates in fact do overlap. If so, the contact point is noted for use by the collision outcome routines (described below). Otherwise, the distance and relative velocity of the two closest and approaching aggregate particles are recorded for use in calculating the next time step. Note that the aggregate rotation is taken into account when calculating the relative velocity, so that collisions can be detected accurately even if the aggregate centers are stationary or moving away from each other.

2.4. Coagulation

Coagulation is actually the simplest particle interaction to model, if it is assumed the contact points are perfectly

rigid. Currently no restructuring or compaction is performed after coagulation (cf. Meakin and Jullien 1988), although this process may be important in the context of planetesimal formation (e.g., Weidenschilling and Cuzzi 1993) and will be investigated in future work. The details of the conditions needed for coagulation to take place, such as surface frost layers (e.g., Hatzes *et al.* 1991; Chokshi *et al.* 1993), similarly are omitted in favor of simpler models for this initial study.

As pointed out in the Introduction, no distinction need be made between particle–cluster aggregation and cluster–cluster aggregation, since both processes are treated analogously. All that is actually required is that the exact cluster orientation be known, but this information is already contained in the principal axes and thus involves little extra work. Moreover, the orientations are updated automatically as part of the collision detection procedure described above.

Once the decision has been made to connect two particles or clusters together, a new particle is created to represent the center of mass of the combined system. If either of the colliding bodies is an aggregate, the corresponding member list is simply linked in to the new particle. Most of the properties (position, velocity, inertia tensor, etc.) of the new aggregate are straightforward to compute, except the spin. To determine the spin, use is made of the fact that the aggregation process must conserve total angular momentum:

$$\mathbf{l}_{after} = \mathbf{l}_{before},\tag{8}$$

where

$$\mathbf{l}_{before} = m_1(\mathbf{r}_1 \times \mathbf{v}_1) + \mathbf{I}_1\omega_1 + m_2(\mathbf{r}_2 \times \mathbf{v}_2) + \mathbf{I}_2\omega_2,\tag{9}$$

$$\mathbf{l}_{after} = M(\mathbf{r} \times \mathbf{v}) + \mathbf{I}\omega.\tag{10}$$

Here the $\mathbf{r}$'s and $\mathbf{v}$'s are positions and velocities, respectively, measured in the space (fixed) frame, and $M = m_1 + m_2$. Note that the position and velocity of the new aggregate correspond to the center of mass values just prior to the impact. Further, the new inertia tensor is given by Eq. (1). Hence ω, the spin of the new aggregate, is the only remaining unknown. Also note that the preceding equations give the spin as seen in the space frame, not the body frame. To obtain the spin with respect to the body axes, write

$$\mathbf{I}\omega = I_1\omega_1\hat{\mathbf{p}}_1 + I_2\omega_2\hat{\mathbf{p}}_2 + I_3\omega_3\hat{\mathbf{p}}_3 = \mathbf{l}_{before} - M(\mathbf{r} \times \mathbf{v}),\tag{11}$$

where I_i, $i = 1, 2, 3$, are the principal moments of inertia of the new aggregate (cf. Section 2.1.2), the $\hat{\mathbf{p}}_i$'s are the corresponding principal axes, and the ω_i's are the desired spin components as seen in the body frame. This equa-

tion can be solved by writing it in the form

$$\mathbf{Mx} = \mathbf{b},\tag{12}$$

where the columns of $\mathbf{M}$ are given by $I_i\hat{\mathbf{p}}_i$, $\mathbf{x} \equiv (\omega_1, \omega_2, \omega_3)$, and $\mathbf{b} \equiv \mathbf{l}_{before} - M(\mathbf{r} \times \mathbf{v})$. The spin vector $\mathbf{x}$ can then be determined using traditional methods of solving linear algebraic equations (e.g., Press *et al.* 1992, Section 2.3: "LU Decomposition").

2.5. Restitution

In Richardson (1994), a fully general scheme for calculating the outcome of point-contact collisions between two uniform spheres was presented. The procedure allowed for inelastic restitution and surface friction. The problem could be solved exactly because the collisions were central; that is, the contact point was on the line connecting the sphere centers. Most aggregate collisions however are oblique, and the problem becomes surprisingly difficult to solve in this case. Part of the difficulty is that it is necessary to specify equations for each unknown impulse component, in addition to the familiar Newtonian equations of motion. Also, it has been recognized that the conventional definitions of restitution and friction coefficients can lead to misleading results in some cases (e.g., Brach 1989, Stronge 1991). These problems can arise in impact configurations that involve nonnegligible tangential impulses and manifest themselves by an *increase* in the post-collision kinetic energy. Fortunately recent work by Brach (1994) and others has led to an approach suitable for certain special cases.

2.5.1. Method of generalized coefficients. The most self-consistent approach to rigid body collision resolution is the method of generalized coefficients (Brach 1994). In this scheme, equations describing the impulse components at the contact point are introduced, each involving a unique coefficient. Together with Newton's second law these equations completely specify the problem, with an equal number of equations as unknowns. The coefficients for the general 3D problem consist of either three kinematic coefficients of restitution or, in the case adopted here, one kinematic coefficient in the normal direction and two transverse *kinetic* coefficients, defined below.

The collision geometry developed in the equations below is illustrated in Figs. 1 and 2. Note that a different notation from that of Brach (1994) has been employed. In particular, all post-collision velocities are denoted by primes ('). A new coordinate system ($\hat{\mathbf{n}}$, $\hat{\mathbf{t}}$, $\hat{\mathbf{p}}$) is defined such that $\hat{\mathbf{n}}$ is a vector perpendicular to the tangent plane at the impact site and points from body 1 to body 2, and $\hat{\mathbf{t}}$, $\hat{\mathbf{p}}$ are in the tangent plane and oriented according to the right-hand rule (Appendix). For a point-contact collision (no moments or couples acting over the contact region),
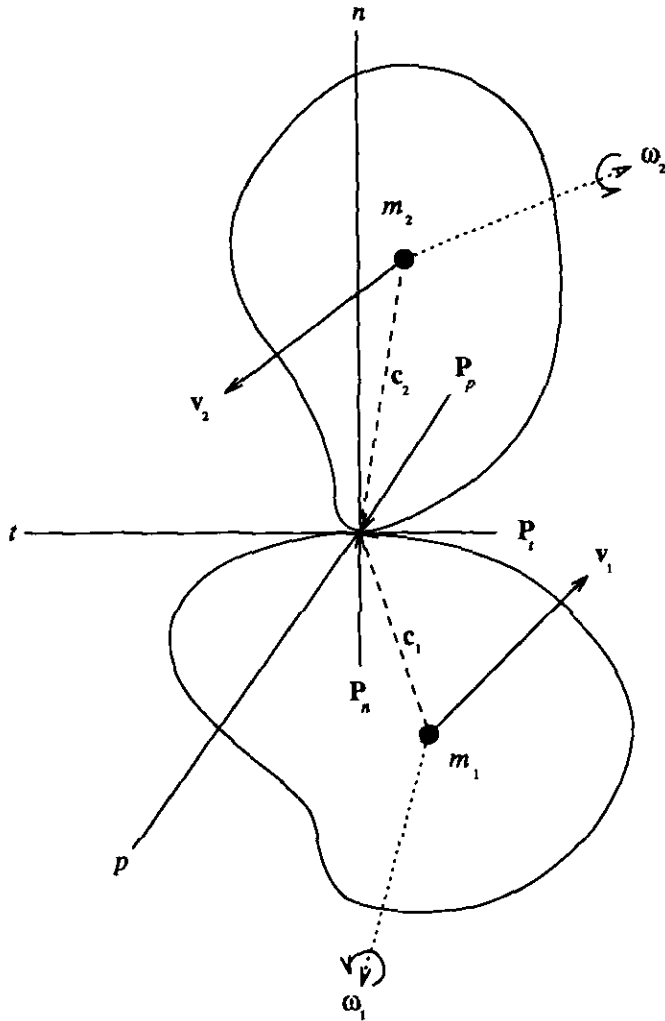
FIG. 1. Diagram illustrating the important components of a 3D point-contact collision between two arbitrary rigid bodies. Refer to text for definitions of the symbols used.

the system equations become

$$m_i\mathbf{v}_i' - m_i\mathbf{v}_i = (-1)^{i-1}\mathbf{P}, \quad i = 1, 2, \tag{13}$$

$$\mathbf{h}_i' - \mathbf{h}_i = \mathbf{c}_i \times (-1)^{i-1}\mathbf{P}, \quad i = 1, 2, \tag{14}$$

$$u_n' = -\varepsilon_n u_n, \tag{15}$$

$$P_t = \mu_t P_n, \tag{16}$$

$$P_p = \mu_p P_n, \tag{17}$$

where $\mathbf{v}_i$ are the center-of-mass velocities, $\mathbf{c}_i$ the relative position vectors of the impact site ($\mathbf{c}_i = \mathbf{r}_c - \mathbf{r}_i$, where $\mathbf{r}_c$ is the position vector of the impact site), $\mathbf{P}$ is the total impulse delivered at the impact site, $\mathbf{u} = \mathbf{v} + \boldsymbol{\sigma}$ is the total relative velocity at the impact site ($\mathbf{v}$ is the relative linear velocity ($\mathbf{v}_2 - \mathbf{v}_1$), $\boldsymbol{\sigma}$ is the relative spin velocity at the impact site ($\boldsymbol{\sigma}_2 - \boldsymbol{\sigma}_1$), and $\boldsymbol{\sigma}_i = \boldsymbol{\omega}_i \times \mathbf{c}_i$), ε_n is the kine-

matic coefficient of restitution, and μ_t, μ_p are the kinetic coefficients for transverse directions. The latter three equations define the restitution coefficients.

When the symbol Δ is introduced to denote the vector difference between a primed quantity and its unprimed counterpart, the first two equations can be combined and cast in simpler form,

$$m_1\Delta\mathbf{v}_1 = -m_2\Delta\mathbf{v}_2, \tag{18}$$

$$\mathbf{I}_i\Delta\boldsymbol{\omega}_i = m_i\mathbf{c}_i \times \Delta\mathbf{v}_i, \quad i = 1, 2, \tag{19}$$

where the angular momenta $\mathbf{h}_i$ have been defined as $\mathbf{I}_i\boldsymbol{\omega}_i$. It is clear by inspection that Eq. (18) conserves linear momentum. It is also straightforward to show that these equations together conserve total angular momentum.

2.5.2. Solution of the collision equations. The best strategy for solving the collision equations is first to find $\mathbf{v}_1'$. The remaining unknowns, $\mathbf{v}_2'$, $\boldsymbol{\omega}_1'$, and $\boldsymbol{\omega}_2'$, follow easily. Start by expanding the kinematic equation ($u_n' = -\varepsilon_n u_n$), and substituting from Eqs. (18) and (19) for $\mathbf{v}_2$ and the angular velocities. It is necessary to multiply Eq. (19) by the inverse matrix $\mathbf{I}_i^{-1}$ to isolate the angular velocities. Note that a convenient vector identity allows $\sigma_{i,n}$ to be written as $\boldsymbol{\omega}_i \cdot (\mathbf{c}_i \times \hat{\mathbf{n}})$, which enables the inverse of the inertia tensor to be taken out from inside the cross product. After a bit of algebra, the following equation is obtained,

$$v_{1,n}' + \mu[\mathbf{I}_2^{-1}(\mathbf{c}_2 \times \mathbf{v}_1')] \cdot (\mathbf{c}_2 \times \hat{\mathbf{n}}) + \mu[\mathbf{I}_1^{-1}(\mathbf{c}_1 \times \mathbf{v}_1')] \cdot (\mathbf{c}_1 \times \hat{\mathbf{n}})$$

$$= v_{1,n} + (1 + \varepsilon_n)\frac{m_2}{M} u_n + \mu [\mathbf{I}_2^{-1}(\mathbf{c}_2 \times \mathbf{v}_1)] \cdot (\mathbf{c}_2 \times \hat{\mathbf{n}})$$

$$+ \mu [\mathbf{I}_1^{-1}(\mathbf{c}_1 \times \mathbf{v}_1)] \cdot (\mathbf{c}_1 \times \hat{\mathbf{n}}), \tag{20}$$

where $M = m_1 + m_2$ is the total mass and $\mu = m_1 m_2/M$ is the reduced mass. To proceed, write all vectors in the ntp basis and let $\mathbf{I}_1^{-1} = (a_{ij})$, $\mathbf{I}_2^{-1} = (b_{ij})$, where $i, j = 1, 2, 3$ (see Appendix). Expand the matrix multiplications and cross products. For example, the term $[\mathbf{I}_2^{-1}(\mathbf{c}_2 \times \mathbf{v}_1')] \cdot (\mathbf{c}_2 \times \hat{\mathbf{n}})$ is given by

$$(c_{2,p}b_{21} - c_{2,t}b_{31})(c_{2,p}v_{1,p}' - c_{2,p}v_{1,t}')$$

$$+ (c_{2,p}b_{22} - c_{2,t}b_{32})(c_{2,p}v_{1,n}' - c_{2,n}v_{1,p}')$$

$$+ (c_{2,p}b_{23} - c_{2,t}b_{33})(c_{2,n}v_{1,t}' - c_{2,t}v_{1,n}').$$

Similar expressions are found for the remaining terms, with particle index 1 replaced by 2 and a replaced by b as appropriate.

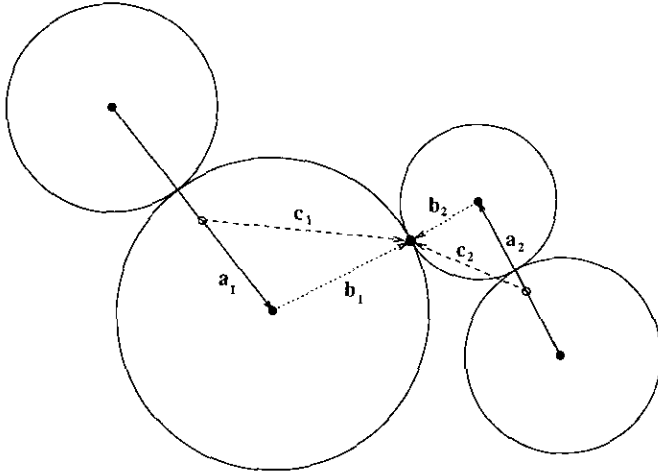Finally, substitute Eq. (13) into (16) and (17) to obtain expressions for $v_{1,t}'$ and $v_{1,p}'$:

FIG. 2. Diagram showing the collision geometry for a pair of aggregates made up of spheres. Each vector c_i connecting the center-of-mass of an aggregate (hollow circle) to the impact point is decomposed into two components: a vector a_i from the aggregate center-of-mass to the center of the impacting sphere (solid point), and a vector b_i from the sphere center to the impact point.

$$v'_{1,t} = v_{1,t} + \mu_t v'_{1,n} - \mu_t v_{1,n}, \tag{21}$$

$$v'_{1,p} = v_{1,p} + \mu_p v'_{1,n} - \mu_p v_{1,n}. \tag{22}$$

It should be emphasized that the derivation to this point is fully general for point-contact collisions. An enormous simplification is possible if it is assumed that all tangential impulses are negligible, i.e., $\mu_t = 0 = \mu_p$. Then terms in $v'_{1,t}$ and $v'_{1,p}$ on the left-hand side of Eq. (20) cancel with identical terms in $v_{1,t}$ and $v_{1,p}$ on the right-hand side. Furthermore, the coefficient of $v'_{1,n}$ on the left-hand side cancels with the coefficient of $v_{1,n}$ on the right-hand side, leaving

$$v'_{1,n} = v_{1,n} + \gamma(1 + \varepsilon_n)\frac{m_2}{M} u_n, \tag{23}$$

where

$$\gamma^{-1} = 1 + \mu(a_{22}c^2_{1,p} - 2a_{23}c_{1,t}c_{1,p} + a_{33}c^2_{1,t} + b_{22}c^2_{2,p}$$
$$- 2b_{23}c_{2,t}c_{2,p} + b_{33}c^2_{2,t}) \tag{24}$$

(the symmetry of the inertia tensors has been exploited here). Expressions for v'_2, ω'_1, and ω'_2 then follow trivially. In summary,

$$\Delta v_1 = \gamma(1 + \varepsilon_n)\frac{m_2}{M} u_n \hat{n}, \tag{25}$$

$$\Delta v_2 = -\gamma(1 + \varepsilon_n)\frac{m_1}{M} u_n \hat{n} \left[= -\frac{m_1}{m_2}\Delta v_1 \right], \tag{26}$$

$$\Delta\omega_1 = m_1 I_1^{-1}(c_1 \times \Delta v_1), \tag{27}$$

$$\Delta\omega_2 = m_2 I_2^{-1}(c_2 \times \Delta v_2) \; [= -m_1 I_2^{-1}(c_2 \times \Delta v_1)]. \tag{28}$$

Again, it is straightforward to show that these equations satisfy conservation of linear and total angular momentum.

If either μ_t or μ_p is nonzero, the expressions become considerably more complex. Furthermore, it is not at all obvious what values should actually be assigned to the tangential coefficients if they are nonzero, since there may exist physical constraints that bound their allowed values, and these may depend on the actual collision geometry. It may be possible to determine the bounding values by applying work–energy conditions, a procedure which is discussed further in Brach (1994) and elsewhere. For the current study, it will be assumed that the tangential impulses are identically zero at the contact point. Note however that rotational motion can still be imparted, since the collisions are generally noncentral.

2.6. Fragmentation

The last collision outcome to be discussed is fragmentation. If the impact energy of a collision involving an aggregate is sufficiently large, or if the impulse delivered to a joint is particularly strong, it is reasonable to suppose that the aggregate may fragment. Thus equilibrium may consist of a competition between coagulation and fragmentation processes (see, e.g., Greenberg et al. 1978, Beaugé and Aarseth 1990, Barge and Pellat 1993, Wetherill and Stewart 1993 for discussion of such equilibria in the context of plaentesimal dynamics).

Although a fully self-consistent model for this process has not yet been constructed, it is instructive to consider the shortcomings of a simplified model in order to understand the complexity of the problem. As a test, a simple model of fragmentation was conceived in which impact energies exceeding a fixed threshold determined solely by the initial energy of the system would result in catastrophic breakup. To carry out the breakup, the impacting aggregates were first coagulated into one body, then the constituent particles of the body were given velocities equal to the vector sum of the center-of-mass velocity of the aggregate, the linear equivalent of the rotational velocity of the constituent particle at the instant of impact, and an outward radial component that accounted for the energy loss in creating the final aggregate just before breakup, simulating the release of some binding energy.

There are two major drawbacks to this model: (1) the release of binding energy is rather ad hoc, and (2) it is unlikely that each bond in the aggregate would be broken. For intermediate impact energies, it is more likely that a distribution of fragments would result, each with differ-

ent sizes, velocities, and spins, according to the nature of the fragment.

A self-consistent model requires a detailed consideration of each bond and would presumably depend on the material involved. Both normal and tangential impulses at each bond site need to be taken into account. The bond model must provide a sink for energy that is converted into mechanical stress and heat. Most important, however, it may be necessary to loosen the rigid body constraint so that collisions are no longer instantaneous. This is because a break near the impact site may prevent a break further on, which suggests a wave propagation model would be most appropriate for the problem. In a recent study, Benz and Asphaug (1994) used a hydrodynamical treatment for the breakup of a solid body. It is hoped, however, that the rigid body approximation can still be used to model the fragmentation of fractal aggregates, and work is currently in progress toward that goal.

3. TEST SIMULATIONS

The results of test runs of the new aggregate code will now be presented. Five models were investigated, each successive model incorporating more features than the previous. This procedure serves to clearly demarcate the contribution of each new feature. Three runs with different random number seeds were performed for each of the first four models and the results were averaged together. Error bars in the plots to follow are the standard deviation of the mean. The fifth model used more particles and was evolved for a longer time; thus only one run was performed. The models are summarized in Table I and will be discussed in detail below.

The simulations were carried out in free space; thus particle trajectories were strictly linear between collisions. In order to maintain a constant particle number (either aggregated or not), periodic boundary conditions were imposed on a cubical simulation region. Ghost par-

ticles were introduced in the surrounding boxes to enable collision detection on the boundaries, in much the same way as described in Wisdom and Tremaine (1988) (also see Richardson 1993). There were two important differences, however: first, since there was no tidal field present, the boxes were not required to slide or shear; second, ghost boxes were needed above and below the plane (i.e., in the $\pm z$ directions) since the vertical extent of the simulation region was finite. This made 26 ghost boxes in all; however, since there was no self-gravity, various simplifications were made to restrict attention to the nearest neighbors (including ghosts) of each particle, as these were the most likely colliders.

The initial conditions were straightforward: the cube was populated with a uniform random distribution of equal-size spheres, with initial velocities also oriented randomly. The velocity magnitudes were either constant or drawn from a Gaussian distribution, depending on the model. The cube had a dimension of 10 in arbitrary units and, in the first four models, the spheres were of radius 0.1. Checks were made to ensure there were no overlapping or touching particles at the start. The center-of-mass position and velocity were subtracted from all particles to give zero net momentum. The particles were also given zero initial spin. The simulations proceeded until some prefixed time in arbitrary units (several CPU hours on an Alpha AXP for most models) and statistics were collected at regular intervals. Information recorded included the collision and merger rate, the mass spectrum, the fractal dimension, volume density, and spin of any aggregates, and the velocity dispersion of the system. Momentum checks were performed on a collision-by-collision basis to ensure that the system remained dynamically self-consistent.

For the purpose of illustration, the impact energy limit for deciding collision outcomes in full restitution models was arbitrarily derived solely from the initial velocity dispersion of the system: impact energies of magnitude less

TABLE I
Summary of the Five Test Models

Model	Number of runs	$N(0)$	R_0	T	Coagulation	Collision outcome
(i)	3	1000	0.1	8.2	Sphere[a]	Coagulation
(ii)	3	1000	0.1	8.2	Sphere[b]	Coagulation
(iii)	3	1000	0.1	8.2	Aggregate	Coagulation
(iv)	3	1000	0.1	8.2	Aggregate	Coagulation or restitution
(v)	1	9000	0.033	40.8	Aggregate	Coagulation or restitution

Note. The initial number of particles, the initial particle size (compared to a fixed box size of 10 arbitrary length units), and the simulation duration (also in arbitrary units) are given as $N(0)$, R_0, and T, respectively. The type of coagulation is either "sphere" (colliding pairs of particles replaced with single spheres) or "aggregate" (colliding particles stick at the point of contact). The collision outcome is either "coagulation" (no restitution) or "coagulation or restitution" (restitution allowed, depending on impact energy).

[a] Particle size and velocity fixed (constant coagulation coefficient).

[b] Particle size and velocity allowed to change (see text).
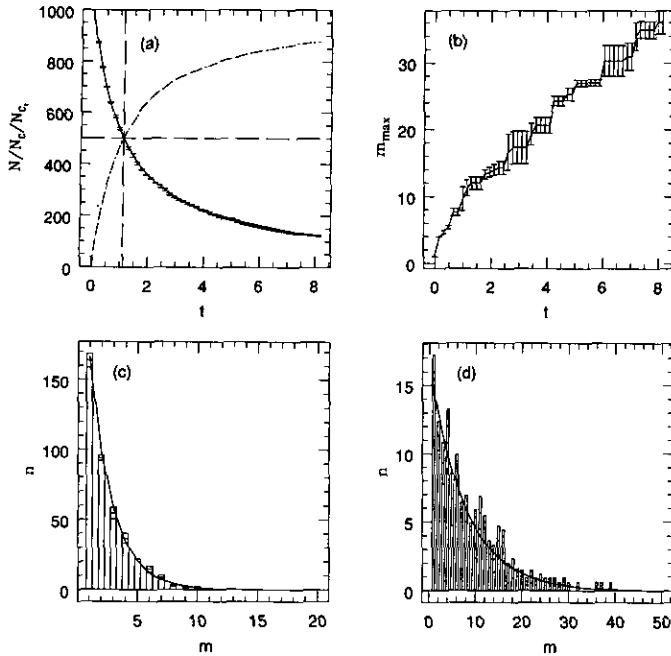
FIG. 3. Plots showing statistics averaged over three test runs of model (i) (cf. Table 1). Error bars are the standard deviation of the mean. (a) gives the number of particles/clusters in the system N (points with error bars), the number of collisions N_C (dotted line), and the number of "first-time" collisions N_{C_1} (dashed line), as a function of time. In this model, which does not include restitution or fragmentation, the latter two curves coincide. The solid line is given by Eq. (30) and is derived from the coagulation equation with constant coagulation coefficient. The long-dashed lines intersect at the point where the number of discrete particles/clusters in the system would be expected to be half the starting value. (b) shows the evolution of the maximum mass in units of the initial mass. The solid line simply connects the points to aid the eye. (c) and (d) show the mass spectrum at times $t = 1.6$ and 8.2 (the end of the simulation), respectively. Error bars are shown at the top of each histogram segment. The solid line is Eq. (31), again derived from the coagulation equation. The plots show that model (i) is in excellent agreement with theory.

than the initial mean kinetic energy resulted in aggregation; impacts exceeding this amount resulted in restitution. This allows the simulation to be scaled to any initial velocity dispersion without appreciably changing the results. The choice of limit was such that roughly half of all collisions resulted in restitution, giving a clear illustration of the effect of bouncing. Ultimately it is desirable to incorporate a model of the aggregate material and surface properties in order to decide the collision outcomes. The normal coefficient of restitution was calculated according to the velocity-dependent formula given by Bridges et al. (1984) for iceballs, scaled to the appropriate units.

Results from model (i) are shown in Figs. 3a–3d. In this model, none of the aggregation formalism was used. Instead, each colliding particle pair was merged into a new single particle with mass equal to the sum of the masses

of the colliding particles. However, the radius of each merged particle was kept fixed at the initial value of 0.1, resulting in a constant collision cross section. In addition, all particles (merged or not) were constrained to have a constant speed. This, together with the fixed cross section, ensured a constant coagulation coefficient, a scenario for which an analytic solution of the coagulation equation is known (Smoluchowski 1916). The discretized coagulation equation is given by

$$\frac{dn_k}{dt} = \frac{1}{2} \sum_{i+j=k} A_{ij} n_i n_j - n_k \sum_{i=1}^{\infty} A_{ik} n_i, \qquad (29)$$

where n_k is the total number of bodies in mass bin k, and A_{ij} is the coagulation coefficient, or "kernel," which is the probability of collision between species i and j per unit time. For model (i), $A_{ij} = \sigma \langle v \rangle / V$, where $\sigma = \pi (2R)^2$ is the collision cross section for identical spheres of radius R, $\langle v \rangle = \frac{4}{3} v_0$ is the mean relative speed between colliders that have constant speed v_0 and random velocity orientation, and V is the volume of the simulation region (the cube of the box size).

Figure 3a shows the number of particles $N(t)$ (points with error bars), the number of collisions $N_C(t)$ (dotted line), and the number of "first-time" collisions $N_{C_1}(t)$ (short-dashed line) as a function of time. Error bars for N_C and N_{C_1} are not shown; the curves for these two quantities consist simply of straight line segments connected between successive data points. The N_{C_1} curve serves to remove consecutive collisions between the same pairs from the total collision count. However, in model (i) each collision resulted in a merger; thus the N_C and N_{C_1} curves overlap exactly. Moreover, $N(t) + N_C(t) = N(0)$, which is emphasized by the symmetry of the curves. The intersection is the point at which half the particles have merged. The solid line which runs through the $N(t)$ points is the analytic solution of the coagulation equation

$$N(t) = N(0) (1 + \tfrac{1}{2} \alpha N(0)t)^{-1}, \qquad (30)$$

where $\alpha = A_{ij}$ is the (constant) coagulation coefficient given above. The curve is an excellent fit to the data. The long-dashed lines intersect at the point $N(t_{1/2}) = N(0)/2$, where $t_{1/2} = 2/\alpha N(0)$.

Figure 3b is a plot of the maximum mass in the system (in units of the initial particle mass) as a function of time. In this case, the solid line merely connects the points. It is difficult to determine the theoretical maximum mass from the coagulation equation because of the ambiguity in the interpretation of fractional values of n_k (see, e.g., the discussion in Wetherill 1990). However, this plot will

be useful for comparison below with models that incorporate fractal aggregation.

Figures 3c and 3d show the mass spectrum of the system at a time near the beginning of the simulation (one-fifth of the way through) and at the end, respectively. Error bars are shown at the top of each histogram segment. The solid line is the analytic solution

$$n_k(f) = N(0)f^2(1 - f)^{k-1}, \qquad (31)$$

where $f \equiv N(t)/N(0)$ is the fraction of particles remaining at time t. Masses are given in units of the initial mass; thus k is equivalent to m in the plots. There is more scatter in 3d than in 3c because of noise due to the smaller number of particles, but allowing for this the data in both plots are in good agreement with theory.

There are only a few known analytic solutions to the coagulation equation (see Wetherill 1990 for a review). As a result, numerical techniques must be used to solve more realistic problems. Nevertheless, the case $A_{ij} = \alpha$ serves as a useful benchmark for comparison of numerical methods. In model (ii) the constraint of constant velocity was removed and particle sizes were allowed to grow with mergers such that the particle density remained constant. The cross section in this case is given by $\sigma_{ij} = \pi(R_i^2 + R_j^2)$. This kind of particle growth model has been used extensively (see, e.g., Weidenschilling 1980, Nakagawa et al. 1981, Beaugé and Aarseth 1990, Aarseth et al. 1993, Richardson 1993). The results are
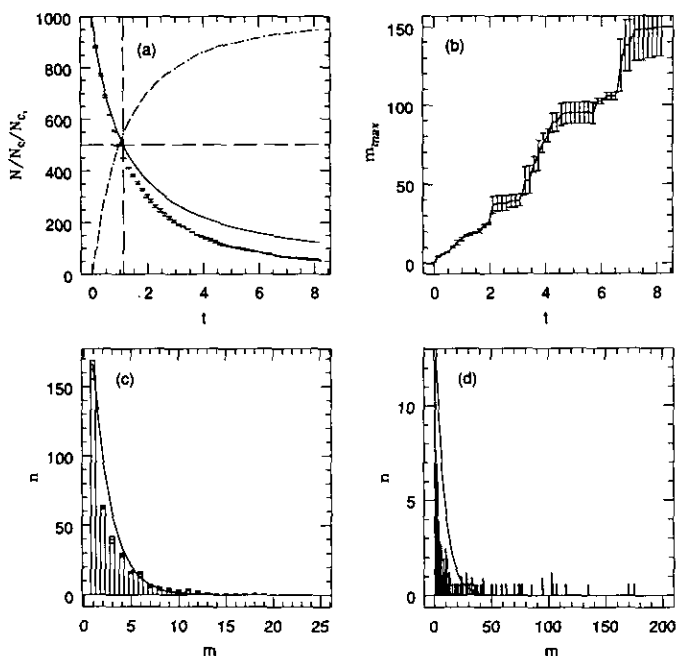
FIG. 5. Run statistics for model (iii), in which "true" aggregation was enabled. Here significant deviations from simple theory are seen, owing to the increased coagulation efficiency of fractal aggregates.

shown in Figs. 4a–4d. The theoretical results for the case of constant coagulation coefficient are also shown for comparison and actually agree quite well with the data. However, the $N(t)$ points lie notably below the theoretical curve, just outside the error bars. In addition, the maximum mass tends to be larger at the end of the simulation. Both trends are indications of the augmented coagulation efficiency which results from the increase of the collision cross section as the particles grow (which slightly exceeds the decrease in velocity dispersion due to energy equipartition). This will be illustrated more dramatically in the following model.

In model (iii) true aggregation was allowed to take place: particles that collided stuck together at the point of contact. The results are shown in Figs. 5a–5d. Although the individual particles remain as discrete components of each aggregate, they are not included in N; thus the particle number still decreases with time. However, N decreases significantly faster in this model than in models (i) and (ii). This indicates that true aggregates collide and grow much more efficiently than single particles, owing to their extended shape. Moreover, the system is susceptible to a kind of runaway accretion, with the formation of a very large particle about 50% larger than the next closest particle in mass (recall that 5d is an average over *three* runs, each run developing a mass on the order of 150 times the initial mass, with the next largest particle being on the order of 100 times the initial mass).
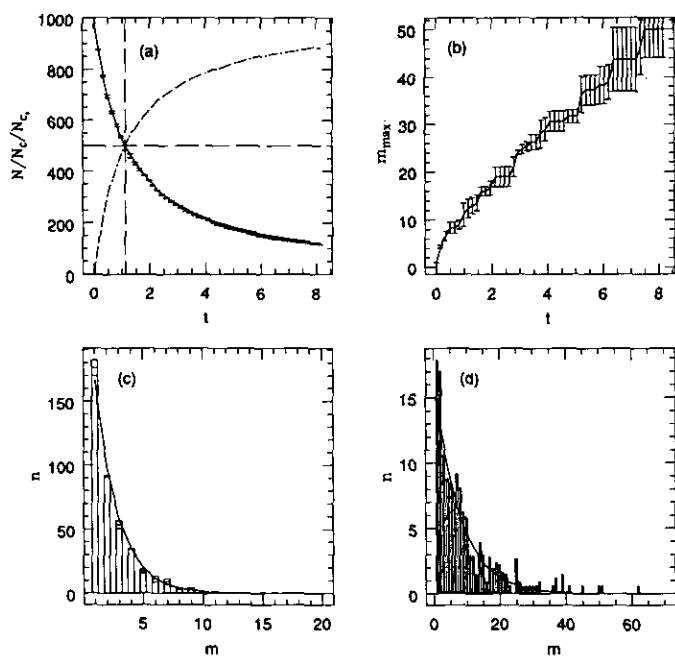

FIG. 4. The same quantities as plotted in Fig. 3 but for model (ii). Although the coagulation coefficient is no longer constant, the model still agrees well with simple theory.
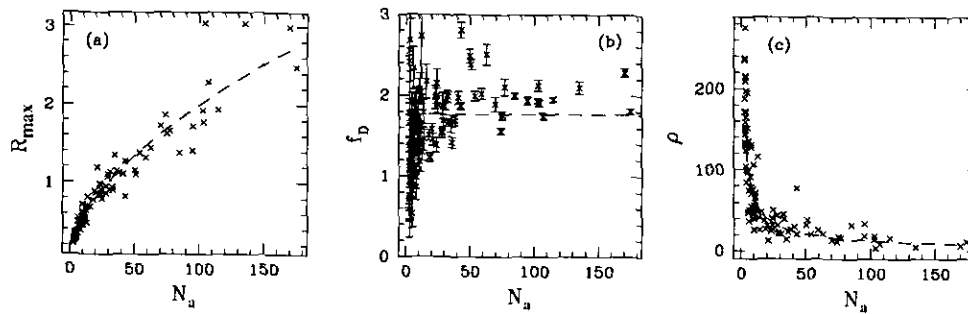
FIG. 6. Plots of model (iii) aggregate properties at the end of the simulation. Points from all three runs are included. In (a), the aggregate size is shown as a function of the number of sphere components. In (b), the distribution of fractal dimensions is shown. The error bars show uncertainties in the derived values. (c) gives the spherically averaged density as a function of particle number. The dashed lines are fits to the data and are described more fully in the text.

The properties of the aggregates in existence at the end of the model (iii) runs are shown in Figs. 6a–6c. In 6a, the quantity R_{max} (cf. Eq. (7)) is shown as a function of the number of particles N_a in each aggregate. The dashed line is a fit to a log–log version of this plot, giving a power-law slope of 0.57 ± 0.01. Hence $R_{max} \propto N_a^{1/2}$ for this system.

In 6b, the fractal dimension f_D is plotted against N_a. The fractal dimension in the current context is defined as the slope of a log–log plot of radius measured from the center of mass vs enclosed particle number (see, e.g., Mandelbrot 1982, for a more general discussion of fractal dimension). Strictly speaking f_D is defined only for objects that extend to infinity. Furthermore, because each aggregate is made up of an integral number of spheres, the number of particles as a function of distance does not vary smoothly. Consequently the values of f_D obtained by the power-law method described above must be considered as only estimates of the true values, and such estimates become increasingly unreliable for the smaller aggregates. This is illustrated by the large uncertainties in f_D for small N_a (shown by error bars). Nevertheless, it can be seen that f_D seems to converge to a mean value near 2 (dashed line) for the larger aggregates, in broad agreement with previous empirical and theoretical studies (see citations in Introduction). The actual mean value of f_D obtained for this model is 1.8 ± 0.4, using inverse square weights. Note that this is close to the inverse of the exponent found in 6a, as would be expected.

The spherically averaged density ρ of the aggregates as a function of N_a is shown in 6c. The density is simply the total mass divided by the volume of a sphere R_{max} in radius. The dashed line is given by $\rho \sim N_a^{-0.71 \pm 0.03}$, where the exponent was determined in the usual way from a log–log plot. If the exponent is labeled γ, it is straightforward to show that the relationship among N_a, R_{max}, and ρ implies that

$$f_D = \frac{3}{1 - \gamma},\qquad(32)$$

which gives $f_D \sim 1.8$, in agreement with the value obtained from 6b.

The effects of restitution collision outcomes on the particle evolution and fractal aggregate properties are investigated in model (iv). The results are plotted in Figs. 7a–7d and Figs. 8a–8c. In Fig. 7a, it is seen that about half again as many collisions take place in this model compared to previous models, owing to the new possibility of an encounter without coagulation. As a consequence, it takes about twice as long to reach the $N(0)/2$ stage in this model. Also, N_C and N_{C_1} no longer coincide, indicating that multiple collisions have occurred between the same two particles/clusters before colliding with other species.
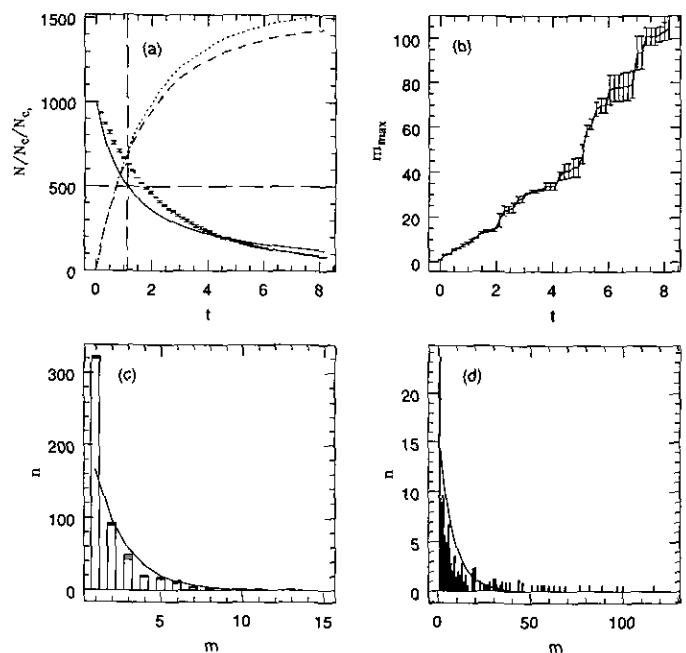

FIG. 7. Run statistics for model (iv), which included the effect of restitution. Here the particle number decreases more slowly than simple theory, owing to the possibility of aggregate bouncing.
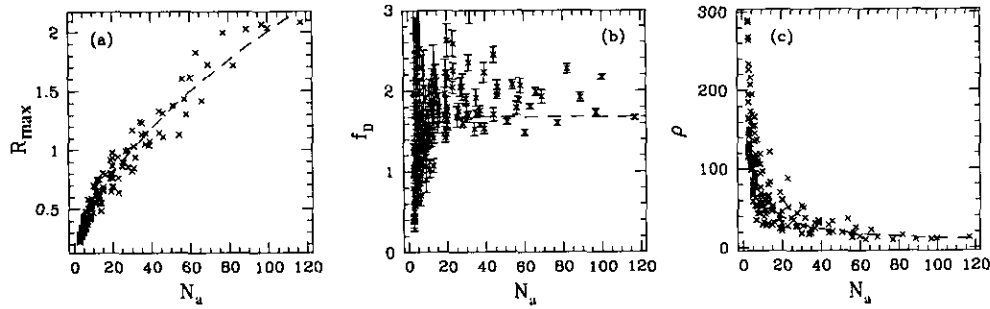
FIG. 8. Aggregate properties for model (iv).

Note that although the system initially evolves more slowly than simple theory (the errorbars lie above the solid curve), eventually the fractal nature of the aggregates ensures that fewer particles remain in the system at the end of the run. On average, there were ~1500 collisions per run in this model, of which 60% resulted in coagulation and 40% in restitution.

The properties of the fractal aggregates formed in model (iv) are similar to those found in the previous model, which suggests that restitution has a minimal effect on the nature of the aggregates formed. The power-law exponent for R_{max} is 0.573 ± 0.009, the mean fractal dimension is 1.7 ± 0.3, and γ is −0.72 ± 0.03.

The last model to be considered, model (v), is identical to model (iv) except that the starting number of particles was increased from 1000 to 9000, the particle size was reduced by a factor of 3, and the system was allowed to evolve for a much longer time. Only one run was performed, requiring less than 1.5 CPU days on an Alpha AXP. The tree code component of box_tree was used to reduce the cost of nearest-neighbor searches, allowing the factor of 9 increase in particle number to be handled in a reasonable time. Since, from the coagulation equation, $t_{1/2} \propto 1/NR^2$, model (v) would be expected to evolve on a time scale similar to that of model (iv). This is confirmed by comparing the usual quantities, plotted in Figs. 9a–9d and Figs. 10a–10c: the half-way stage was reached at $t \sim 1.7$, and approximately 90% of the mass was aggregated by $t \sim 8.2$, similar to model (iv). During the course of the run, there were 14420 collisions, of which 62% resulted in coagulation and 38% in restitution. At the end of the simulation, 99.98% of the mass was aggregated, with one cluster accounting for 31% of the total mass. Note that there were several large merger events in the latter half of the run (Fig. 9b). At the end of the simulation, the aggregate properties were (Fig. 10) R_{max} exponent = 0.52 ± 0.01, mean f_D = 2.0 ± 0.2, and γ = −0.55 ± 0.04. The larger particles dominate the average properties in this case, since there were fewer unaccreted particles at the end of the run.

The evolution of the space components of the system velocity dispersion in model (v) is shown in Fig. 11a. The dispersions decrease monotonically as they must since there was no energy source in the simulation. Furthermore the system remains essentially isotropic, in accordance with the symmetry of the initial conditions and the simulation environment itself. Figure 11b shows the total kinetic energy (translational plus rotational) as a function of particle mass at $t \sim 8.2$ (the termination point of the earlier models), when there were still a fair number of discrete particles/clusters. It can be seen from the plot
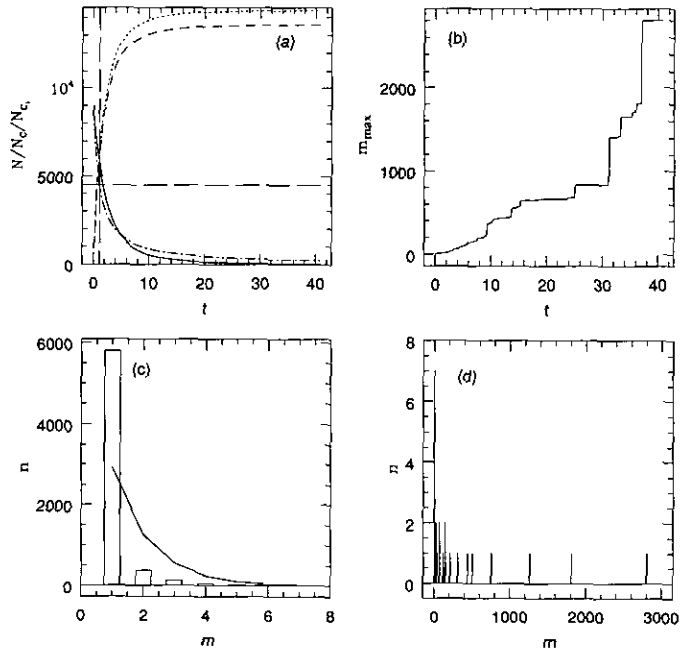

FIG. 9. Run statistics for model (v). This model was similar to model (iv) but had a larger starting particle number, used smaller particles, and was allowed to run for a longer time. Only one run was performed; the solid line in (a) in this case is the observed number of particles while the dot–dashed line gives the simple theoretical prediction for comparison. The theoretical curve in (d) has been omitted for clarity. By the end of the simulation, 99.98% of the mass is in aggregates.
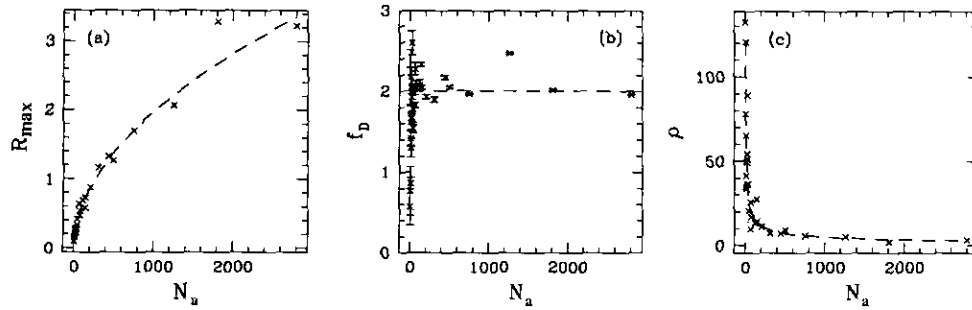
FIG. 10.   Aggregate properties for model (v), at $t \sim 40.8$, the end of the run.

that the system is in good equipartition. In other words, the larger an aggregate, the smaller its velocity and spin with respect to its less massive neighbors. This trend continues throughout the simulation but with increased scatter due to the smaller number of particles.

The final figure, Fig. 12, is a ray-traced diagram of the second largest aggregate at the end of the model (v) run. The aggregate is made up of 1811 spheres and has a fractal dimension of 2.02 ± 0.01. Although the overall shape of the aggregate is linear, the constituent particles are tightly clustered around the curved long axis, giving rise to a fractal dimension near 2. Note that size differences between spheres are a result of viewing perspective, not of any intrinsic size distribution. The qualitative form of this aggregate compares favorably with results of other authors (see, e.g., Blum *et al.* 1994 for a recent example), though there are more gaps and irregular features in the aggregate shown here, owing to the dynamical growth method used.

4. CONCLUSIONS

A new numerical method for the self-consistent treatment of fractal aggregate dynamics has been presented. The method allows for the rigid body rotation of the aggregates in accordance with Euler's equations. Three collision outcomes were considered: coagulation, restitution, and fragmentation, although only the first two models were tested in detail. The restitution treatment required the use of generalized impact coefficients to handle oblique collisions in a consistent manner. Test simulations were discussed, illustrating various aspects of the new code and showing excellent agreement with analytic theory. Although the tests only included equal-size particles, the code allows for an arbitrary distribution of particle sizes. It is hoped that tangential impulses, compaction, and a proper fragmentation model will be incorporated in the future.

The tests demonstrate the feasibility of direct simulation of particle aggregate dynamics. This level of sophis-

tication is now possible because of the rapidly increasing power of low-cost workstations at astronomical institutions. As a result, more and more relevant physics can be included in simulations of complicated regimes such as the early solar nebula, planetary rings systems, and the interstellar medium.

The next stage of investigation involves applying the code to one of these regimes. Of particular interest is a study of the optical properties of dust-like aggregates. Effects to be modeled include the absorption, scattering, polarization, and possibly sputtering properties of such aggregates. There is code already available for investigating some of these optical properties (e.g., Draine and Flatau 1994). Another important consideration is the effect of gas drag and tidal fields on aggregate dynamics. These aspects would require a treatment of torque (cf. Eq. (4)) and would therefore represent a significant increase in the complexity of the problem. However, as the aggregate code was built within box_tree, the machinery for careful integration in the presence of time-varying forces is already in place.

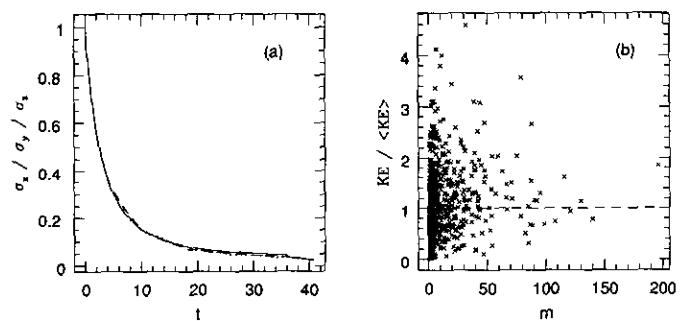It is hoped that the work presented here will provide a

FIG. 11.   (a) shows the evolution of the velocity dispersion in model (v). All three Cartesian components are shown but they overlap due to the isotropy of the system. (b) shows the total kinetic energy (translational plus rotational) as a function of particle mass for all the particles/clusters in model (v) at $t \sim 8.2$. The distribution of points shows that the system is in rough energy equipartition.

FIG. 12. Ray-traced diagram showing the configuration of the largest aggregate at the end of the model (v) run. The aggregate contains 1811 particles and has a fractal dimension nearly equal to 2. Note that apparent size differences between spheres in this diagram are simply a consequence of the 3D viewing geometry.

bridge to even more sophisticated simulations of some of the complex astrophysical systems that up to now have had to be treated statistically. The code is freely available to any researchers who would like to use it and can be obtained by request to the author.

APPENDIX

Collision Geometry: The *ntp* Basis

It is particularly simple to characterize the geometry of collisions between aggregates of spheres. A single point contact between such aggregates can only involve two spheres, one from each aggregate (Fig. 2). The *ntp* basis is constructed by choosing $\hat{n}$ to lie along the vector $\mathbf{b}_i$ in the figure. Then $\hat{t}$ and $\hat{p}$ can be formed using the familiar Gram-Schmidt orthonormalization procedure (described in any elementary linear algebra text).

To solve Eq. (20), the a's and b's representing the inverse matrices $\mathbf{I}_1^{-1}$ and $\mathbf{I}_2^{-1}$ must first be transformed to the *ntp* basis. To accomplish this, let $\mathbf{A}$ be a matrix whose columns are the principal axes of the body in question. If $\mathbf{I}_{body}$ is the inertia tensor in the body frame (i.e., a diagonal matrix whose elements are the principal moments of inertia), then the inertia tensor in the space frame is given by

$$\mathbf{I}_{space} = \mathbf{A}\mathbf{I}_{body}\mathbf{A}^T.$$

Similarly, if **B** is a matrix whose columns are the unit vectors $\hat{\mathbf{n}}$, $\hat{\mathbf{t}}$, and $\hat{\mathbf{p}}$,

$$\mathbf{I}_{space} = \mathbf{B}\mathbf{I}_{ntp}\mathbf{B}^T,$$

where $\mathbf{I}_{ntp}$ is the inertia tensor in the ntp basis. Since the columns of **B** form an orthonormal basis set, **B** is orthogonal and therefore invertible, and the inverse is equal to the transpose. Hence

$$\mathbf{I}_{ntp} = \mathbf{B}^T\mathbf{A}\mathbf{I}_{body}\mathbf{A}^T\mathbf{B}. \tag{33}$$

It remains to invert the matrix, which can be accomplished using traditional numerical methods (e.g., Press *et al.* 1992, Section 2.3).

ACKNOWLEDGMENTS

REFERENCES

AARSETH, S. J. 1985. Direct methods for *N*-body simulations. In *Multiple Time Scales* (J. U. Brackill and B. I. Cohen, Eds.), pp. 377–418. Academic Press, New York.

AARSETH, S. J., D. N. C. LIN, AND P. L. PALMER 1993. Evolution of planetestimals. II. Numerical simulations. *Astrophys. J.* **403**, 351–376.

ASPHAUG, E., AND W. BENZ 1994. Density of Comet Shoemaker–Levy 9 deduced by modelling breakup of the parent "rubble pile." *Nature* **370**, 120–124.

BACKMAN, D. E., AND F. PARESCE 1993. Main-sequence stars with circumstellar solid material: The Vega phenomenon. In *Protostars and Planets III* (E. H. Levy and J. I. Lunine, Eds.), pp. 1253–1304. Univ. of Arizona Press, Tucson.

BARGE, P., AND R. PELLAT 1993. Mass spectrum and velocity dispersions during planetesimal accumulation. II. Fragmentation. *Icarus* **104**, 79–96.

BEAUGÉ, C., AND S. J. AARSETH 1990. *N*-body simulations of planetary formation. *Mon. Not. R. Astron. Soc.* **245**, 30–39.

BENZ, W., AND E. ASPHAUG 1994. Impact simulations with fracture. I. Method and tests. *Icarus* **107**, 98–116.

BLUM, J., TH. HENNING, V. OSSENKOPF, R. SABLOTNY, R. STOGNIENKO, AND E. THAMM 1994. Fractal growth and optical behaviour of cosmic dust. In *Fractals in the Natural and Applied Sciences* (A-41) (M. M. Novak, Ed.), pp. 47–59. Elsevier Amsterdam.

BLUM, J., AND M. MÜNCH 1993. Experimental investigations on aggregate–aggregate collisions in the early solar nebula. *Icarus* **106**, 151–167.

BOSS, A. P., AND J. A. GRAHAM 1993. Clumpy disk accretion and chondrule formation. *Icarus* **106**, 168–178.

BRACH, R. M. 1989. Rigid body collisions. *J. Appl. Mech.* **56**, 133–138.

BRACH, R. M. 1994. Formulation of rigid body impact problems using generalized coefficients. *J. Appl. Mech.*, submitted.

BRIDGES, F. G., A. HATZES, AND D. N. C. LIN 1984. Structure, stability, and evolution of Saturn's rings. *Nature* **309**, 333–335.

CHOKSHI, A., A. G. G. M. TIELENS, AND D. HOLLENBACH 1993. Dust coagulation. *Astrophys. J.* **407**, 806–819.

CUZZI, J. N., A. R. DOBROVOLSKIS, AND J. M. CHAMPNEY 1993. Particle–gas dynamics in the midplane of a protoplanetary nebula. *Icarus* **106**, 102–134.

CUZZI, J. N., J. J. LISSAUER, L. W. ESPOSITO, J. B. HOLBERG, E. A. MAROUF, G. L. TYLER, AND A. BOISCHOT 1984. Saturn's rings: Properties and processes. In *Planetary Rings* (R. Greenberg and A. Brahic, Eds.), pp. 73–199. Univ. of Arizona Press, Tucson.

DONN, B. D. 1990. The formation and structure of fluffy cometary nuclei from random accumulation of grains. *Astron. Astrophys.* **235**, 441–446.

DRAINE, B. T., AND P. J. FLATAU 1994. Discrete-dipole approximation for scattering calculations. *J. Opt. Soc. Am. A* **11**, 1491–1499.

GOLDREICH, P., AND W. R. WARD 1973. The formation of planetesimals. *Astrophys. J.* **183**, 1051–1061.

GOLDSTEIN, H. 1980. *Classical Mechanics*, 2nd ed. Addison–Wesley, Reading, MA.

GREENBERG, R., J. F. WACKER, W. K. HARTMANN, AND C. R. CHAPMAN 1978. Planetesimals to planets: Numerical simulation of collisional evolution. *Icarus* **35**, 1–26.

GROSSMAN, J. N. 1988. Formation of chondrules. In *Meteorites and the Early Solar System* (J. F. Kerridge and M. S. Matthews, Eds.), pp. 680–696. Univ. of Arizona Press, Tucson.

HATZES, A. P., F. BRIDGES, D. N. C. LIN, AND S. SACHTJEN 1991. Coagulation of particles in Saturn's rings: Measurements of the cohensive force of water frost. *Icarus* **89**, 113–121.

KLAVETTER, J. J. 1989. Rotation of Hyperion. II. Dynamics. *Astron. J.* **98**, 1855–1873.

LIFFMAN, K. 1992. A direct simulation Monte-Carlo method for cluster coagulation. *J. Comput. Phys.* **100**, 116–127.

LUMME, K., AND W. M. IRVINE 1979. A model for the azimuthal brightness variations in Saturn's rings. *Nature* **282**, 695–696.

MANDELBROT, B. B. 1982. *The Fractal Geometry of Nature*. Freeman, San Francisco.

MEAKIN, P., AND B. DONN 1988. Aerodynamic properties of fractal grains: Implications for the primordial solar nebula. *Astrophys. J.* **329**, L39–41.

MEAKIN, P., AND R. JULLIEN 1988. The effects of restructuring on the geometry of clusters formed by diffusion-limited, ballistic, and reaction-limited cluster–cluster aggregation. *J. Chem. Phys.* **89**, 246–250.

NAKAGAWA, Y., K. NAKAZAWA, AND C. HAYASHI 1981. Growth and sedimentation of dust grains in the primordial solar nebula. *Icarus* **45**, 517–528.

OSSENKOPF, V. 1993. Dust coagulation in molecular clouds: The formation of fluffy aggregates. *Astron. Astrophys.* **280**, 617–646.

PALME, H., AND W. V. BOYNTON 1993. Meteoritic constraints on conditions in the solar nebula. In *Protostars and Planets III* (E. H. Levy and J. I. Lunine, Eds.), pp. 979–1004. Univ. of Arizona Press, Tucson.

PRESS, W. H., S. A. TEUKOLSKY, W. T. VETTERLING, AND B. P. FLANNERY 1992. *Numerical Recipes in C: The Art of Scientific Computing*, 2nd ed. Cambridge Univ. Press, Cambridge, UK.

RICHARDSON, D. C. 1993. A new tree code method for simulation of planetesimal dynamics. *Mon. Not. R. Astron. Soc.* **261**, 396–414.

RICHARDSON, D. C. 1994. Tree code simulations of planetary rings. *Mon. Not. R. Astron. Soc.* **269**, 493–511.

SAFRONOV, V. S. 1969. *Evolution of the Protoplanetary Cloud and the Formation of the Earth and Planets.* Nauka Press, Moscow.

SALO, H. 1994. Simulations of dense planetary rings III: Self-gravitating identical particles. *Icarus*, submitted.

SMOLUCHOWSKI, M. 1916. Drei Vortrage über Diffusion. Brownsche Molekularbewegung und Koagulation von Kolloidteilchen. III. Theorie der Koagulation. *Phys. Zeit.* **17**, 593–599.

SHOWALTER, M. R., AND P. D. NICHOLSON 1990. Saturn's rings through a microscope: Particle size constraints from the Voyager PPS scan. *Icarus* **87**, 285–306.

SOLEM, J. C. 1994. Density and size of Comet Shoemaker–Levy 9 deduced from a tidal breakup model. *Nature* **370**, 349–351.

STRONGE, W. J. 1991. Friction in collisions: Resolution of a paradox. *J. Appl. Phys.* **69**, 610–612.

WEIDENSCHILLING, S. J. 1980. Dust to planetesimals: Settling and coagulation in the solar nebula. *Icarus* **44**, 172–189.

WEIDENSCHILLING, S. J. 1994. Origin of cometary nuclei as "rubble piles." *Nature* **368**, 721–723.

WEIDENSCHILLING, S. J., AND J. N. CUZZI 1993. Formation of planetesimals in the solar nebula. In *Protostars and Planets III* (E. H. Levy and J. I. Lunine, Eds.), pp. 1031–1060. Univ. of Arizona Press, Tucson.

WEIDENSCHILLING, S. J., B. DONN, AND P. MEAKIN 1989. The physics of planetesimal formation. In *The Formation and Evolution of Planetary Systems* (H. A. Weaver and L. Danly, Eds.), pp. 131–150. Cambridge Univ. Press, Cambridge, UK.

WETHERILL, G. W. 1990. Comparison of analytical and physical modeling of planetesimal accumulation. *Icarus* **88**, 336–354.

WETHERILL, G. W., AND G. R. STEWART 1993. Formation of planetary embryos: Effects of fragmentation, low relative velocity, and independent variation of eccentricity and inclination. *Icarus* **106**, 190–209.

WISDOM, J., AND S. TREMAINE 1988. Local simulations of planetary rings. *Astron. J.* **95**, 925–940.